Proceedings of the Canadian Society for Mechanical Engineering International Congress
Computational Fluid Dynamics Canada International Congress
CSME - CFD-SC2023
May 28-31, 2023, Sherbrooke, QC, Canada

Near-Field Aero-Acoustic Shape Optimization at Low Reynolds Number

Mohsen Hamedi *, Brian C. Vermeire

Department of Mechanical, Industrial, and Aerospace Engineering, Concordia University, Montreal, Canada
*mohsen.hamedi@concordia.ca

***Abstract*—**The Flux Reconstruction (FR) approach, is used to study the flow over two-dimensional objects at low Reynolds numbers. The Sound Pressure Level (SPL) is computed using a direct acoustic approach at an observer in the near field. The aero-acoustic shape optimization is performed using the gradient-free Mesh Adaptive Direct Search (MADS) technique. NACA 4-digit airfoil is optimized at $Re = 10,000$ and $M_\infty = 0.2$ to reduce the trailing edge noise. The airfoil's shape is optimized at an appropriate angle of attack to reduce the SPL while increasing the lift coefficient. The optimized airfoil is quiet with $0\ dB$ noise and the lift coefficient is increased by more than 80%.

***Keywords-component*—gradient-free; optimization; near-field; aero-acoustic; high-order; noise reduction.**

I. Introduction

According to the World Health Organization (WHO), noise-induced diseases cause a loss of over one million healthy life years annually in Western Europe [1]. Previous studies have examined the adverse effects of noise on the environment and human health [2], such as wildlife disturbance and habitat loss [3], and hearing impairment, sleep disruption, stress and cardiovascular disease [2]. With the expected doubling of air passengers by 2040 [4], aviation noise impacts need to be addressed and mitigated.

Accurate aviation noise reduction requires both a precise noise prediction technique and a suitable optimization strategy. The computational challenges specific to aeroacoustics include numerical dispersion and dissipation, outflow and wall boundary conditions, the capacity to model non-linear phenomena, and the ability to accurately resolve various length scales [5, 6]. The latest evolution of CAA has been reviewed thoroughly by different researchers [7, 8, 9]. The advances in high-order numerical techniques is promising for CAA. These high-order techniques, such as Spectral Difference (SD) [10], Spectral Volume (SV) [11], and FR [12], amongst others, demonstrate great potential for CAA due to their minimal numerical errors [13] and suitability for modern hardware architectures [14].

Optimization techniques play a crucial role in various fields of engineering and science, including fluid dynamics, aerodynamics, and aero-acoustics, to find the optimal solution for a problem by minimizing or maximizing an objective function. These techniques can be classified into gradient-based and gradient-free methods. Gradient-based optimization techniques require accurate calculation of the objective function's gradient to iteratively find the optimum. For unsteady problems, gradient-based optimization methods may not be useful as the objective function will be noisy and non-smooth. In these cases, gradient-free optimization methods are often more suitable, as they can handle noisy and complex objective functions. The combination of gradient-free optimization techniques and high-performance computing technologies has led to new possibilities for optimizing fluid dynamics problems related to noise reduction in aviation and engineering systems.

In this study, the Discontinuous Galerkin (DG) method, recovered via FR, is used. Moreover, the sound pressure level at an observer location is computed. Then, the shape optimization procedure is conducted using the gradient-free MADS technique to reduce the noise at the observer. The objective of this study is to investigate the feasibility of high-order numerical techniques coupled with gradient-free optimizers for aero-acoustic problems.

II. Methodology

This section presents an overview of the methodology employed to solve the unsteady Navier-Stokes equations, followed by an explanation of the optimization technique used in this study.

A. Governing Equations

The compressible unsteady non-linear Navier-Stokes equations can be cast in the following general form

$$\frac{\partial U}{\partial t} + \nabla \cdot F = 0, \tag{1}$$

where U is the vector of conserved variables

$$U = \begin{bmatrix} \rho \\ \rho u_i \\ \rho E \end{bmatrix}, \tag{2}$$

where ρ is density, ρu_i is a component of the momentum, and ρE is the total energy. The inviscid and viscous Navier-Stokes fluxes are

$$F_{i,j}(U) = \begin{bmatrix} \rho u_j \\ \rho u_i u_j + \delta_{ij} p \\ u_j(\rho E + p) \end{bmatrix}, \tag{3}$$

and

$$F_{\nu,j}(U, \nabla U) = \begin{bmatrix} 0 \\ \tau_{ij} \\ -q_j - u_i \tau_{ij} \end{bmatrix}, \tag{4}$$

respectively, where δ_{ij} is the Kronecker delta. The pressure is determined via the ideal gas law as

$$p = (\gamma - 1)\rho \left(E - \frac{1}{2} u_k u_k \right), \tag{5}$$

where γ is the ratio of the specific heat at constant pressure, c_p, to the specific heat at constant volume, c_v. The viscous stress tensor is

$$\tau_{ij} = \mu \left(\frac{\partial u_i}{\partial x_j} + \frac{\partial u_j}{\partial x_i} - \frac{2}{3} \frac{\partial u_k}{\partial x_k} \delta_{ij} \right). \tag{6}$$

And, the heat flux is

$$q_j = -\frac{\mu}{Pr} \frac{\partial}{\partial x_j} \left(E + \frac{p}{\rho} - \frac{1}{2} u_k u_k \right), \tag{7}$$

where μ is the dynamic viscosity and Pr is the Prandtl number.

B. Flux Reconstruction

The FR approach is a high-order accurate numerical method first introduced by Huynh [12] in 2007. It is appealing due to its accuracy, generality, robustness, and suitability for modern hardware architectures [14]. The FR framework is explained here in multiple dimensions, following Wang's formulation [15].

Consider the general form of the hyperbolic conservation law

$$\frac{\partial U}{\partial t} + \nabla . F = 0. \tag{8}$$

In the FR approach, the continuous domain is divided into a number of elements with a set of discrete solution points within each element. In this study, the solution and flux points are located at tensor products of Gauss points. The discretized governing equations are solved numerically within each element, Ω_k. We assume that U_k^δ is the approximated solution to U within element k, and the solution is in the space of polynomials of degree $\mathcal{P}$ or less, i.e., $U_k^\delta \in \mathbb{P}^\mathcal{P}$. This approximate solution is allowed to be discontinuous across cell interfaces. Thus, a common Riemann flux must be defined to replace the normal flux. In this study, a Rusanov/Lax-Friedrichs flux is used at the interface between elements. By defining a correction field, $G_k \in \mathbb{P}^\mathcal{P}$, 8 is re-written as

$$\frac{\partial U_k^\delta}{\partial t} + \nabla \cdot F\left(U_k^\delta\right) + G_k = 0, \tag{9}$$

which is satisfied within the element Ω_k. In this study, the DG method is recovered via the FR formulation by choosing nodal basis functions as the weighting function [15], and the Rusanov and second method of Bassi and Rebay (BR2) are used for the common inviscid and viscous flux.

C. Mesh Adaptive Direct Search Optimization

The goal of an optimization problem is to find the design variables that minimize or maximize a scalar quantity, known as the objective function, $\mathcal{F}$. The design variables, $\boldsymbol{\mathcal{X}}$, are the unknown parameters of the system being optimized and are used to describe the solution of the optimization problem. The initial guess, $\boldsymbol{\mathcal{X}}_0$, provides a starting point for the optimization algorithm to begin its search for the optimal solution. The quality of the initial guess can significantly impact the convergence and efficiency of the optimization process. The optimization problem is terminated when the stopping criteria is met. The computational cost of the gradient-free optimization techniques increases drastically by increasing the number of design parameters. However, the gradient-free optimization techniques are relatively robust and flexible design strategies and an exciting candidate for noisy objective functions since the sensitivities of the objective function is not required. The computational cost of gradient-free optimization techniques can be reduced by implementing the FR method, which results in more accurate results at a lower computational cost in comparison to other high-order methods.

III. Numerical Example

This section focuses on investigating the aero-acoustic shape optimization of two-dimensional NACA 4-digit airfoil. The aerodynamic characteristics of the NACA0012 airfoil have been extensively studied through experiments [16, 17] and CFD simulations [18, 19]. The study of airfoil noise dates back to the 1970s when several experimental studies showed that discrete tones are emitted from isolated airfoils [20, 21], and other researchers focused on understanding this phenomenon [16, 22]. The shape of the airfoil is optimized for noise reduction of the high-lift devices [23], laminar flow trailing edge [24], and turbulent flow trailing edge [25]. This study examines the laminar flow trailing edge and the aero-acoustic shape optimization of the NACA0012 airfoil at a low Reynolds number, $Re = 10,000$, which is the operating regime for UAVs.

A. Validation

In this section, the flow over a two-dimensional NACA0012 airfoil is validated. A grid-resolution-independence study is performed for the time-averaged lift and drag coefficients,

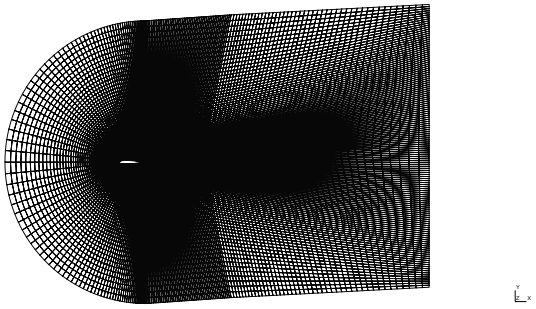

(a) The computational domain.

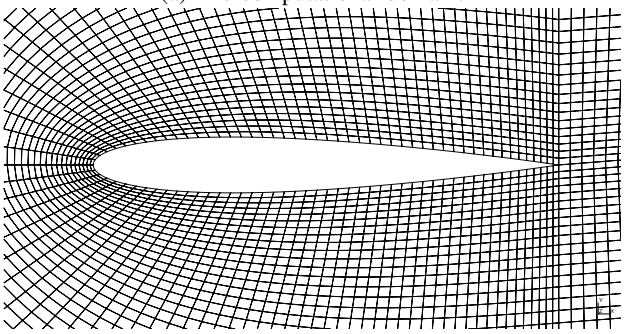

(b) The vicinity of the airfoil.

Figure. 1: The computational grid for NACA0012 airfoil at $\alpha = 3^{\circ}$.

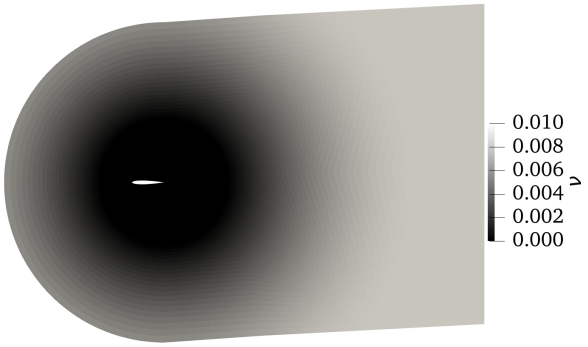

(a) The artificial diffusion.

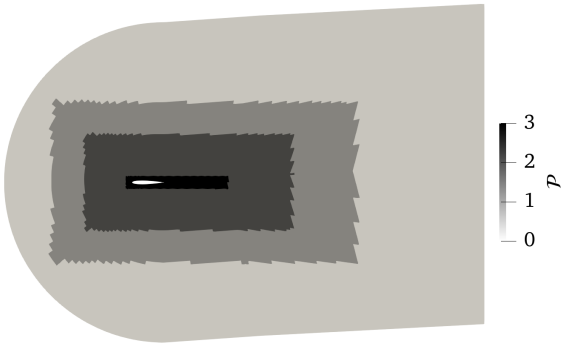

(b) The polynomial distribution.

Figure. 2: The boundary treatments.

and the sound pressure level at an observer located a unit chord length above the trailing edge. The time-averaged lift coefficient is compared with reference DNS data [26] to validate the simulation.

1) Computational Details: The computational grid consists of $19,596$ quadrangular elements, depicted in Figure 1. The domain is extended to $5c$ in the y-direction and to $10c$ in the x-direction, where $c = 1$ is the chord length of the airfoil. The stretching ratio is kept below 5% everywhere in the domain. The elements in the wake region are inclined at the angle of attack to capture the vortices behind the trailing edge. The computational domain is shown in Figure 1. The Reynolds number for this study is $Re = 10,000$, the inflow Mach number is $M_{\infty} = 0.2$, the angle of attack is 3 degrees, and the Prandtl number is $Pr = 0.71$. The simulation is run for 60 convective times, and flow statistics are averaged for the last 20 convective times. The second-order Paired Explicit Runge-Kutta (P-ERK) temporal scheme [27] is used to advance the solution in time.

Vortices leaving the computational domain can generate non-physical acoustic wave reflections off the boundaries, contaminating the solution. Thus, the strength of such vortices must be decreased to eliminate the acoustic wave reflections off the boundaries. The addition of artificial diffusion and variable solution polynomial degrees are used in this study, shown in Figure 2. Artificial diffusion is applied beyond a circle with a radius of $2c$ centered at the trailing edge. Its magnitude increases to a maximum of 0.01 and a radius of $8c$ using a sinusoidal function. The solution polynomial distribution is shown in Figure 2b, where in the vicinity of the airfoil $\mathcal{P} = 3$ and it decreases to zero close to the boundaries.

2) Results and Discussion: A different set of variable polynomial degrees are used to study the independence of the results to the grid resolution. Three different mesh resolutions are used with a maximum polynomial degree of $\mathcal{P}2$, $\mathcal{P}3$, and $\mathcal{P}4$. The time-averaged lift and drag coefficients are computed along with the sound pressure level at the observer located a unit chord length above the trailing edge and compared using three different grid resolutions, shown in Table I. The time-averaged lift coefficient differs by less than 0.4% when the highest polynomial degree in the domain is $\mathcal{P}4$ compared to that of $\mathcal{P}3$, while the time-averaged drag coefficient remains the same by increasing the grid resolution. The time-averaged lift coefficient obtained via the $\mathcal{P}0 - \mathcal{P}3$ simulation agrees well with the DNS data [26]. Furthermore, the sound pressure level difference between $\mathcal{P}0 - \mathcal{P}3$ and $\mathcal{P}1 - \mathcal{P}4$ simulations is $0.53\ dB$ or 0.48%. Thus, it is concluded that the grid resolution for $\mathcal{P}0-\mathcal{P}3$ simulation is sufficient for this problem.

The sensitivity of the time-averaged quantities to the averaging window is investigated by choosing two different averaging windows. The lift and drag coefficients are averaged over 20 and 40 convective time windows, shown in Table II. The difference between the time-averaged lift and drag coefficients for both averaging window lengths is negligible. Thus, the quantities are averaged over a 20 convective time window.

TABLE. I: Averaged lift and drag coefficients and the sound pressure level measured at a unit chord distance above the trailing edge of the baseline NACA0012.

	$\mathcal{P}0-\mathcal{P}2$	$\mathcal{P}0-\mathcal{P}3$	$\mathcal{P}1-\mathcal{P}4$
$\overline{C_L}$	0.0877	0.0886	0.0889
$\overline{C_D}$	0.0448	0.0447	0.0447
SPL	109.59 dB	110.00 dB	110.53 dB

TABLE. II: Averaging window sensitivity of the time-averaged quantities.

	20 t_c	40 t_c
$\overline{C_L}$	0.08857	0.08863
$\overline{C_D}$	0.04472	0.04473

The time history of lift and drag coefficients are shown in Figure 3 for the last two convective times. The periodic behaviour of C_L and C_D is associated to the periodic vortex shedding at the trailing edge.
The pressure perturbation at $t_c = 60$ is shown in Figure 6a. Acoustic waves are generated close to the trailing edge and propagate everywhere in the domain. There are no visible acoustic wave reflections off the boundaries, showing the effectiveness of boundary treatments used in this study. The amplitude of the pressure perturbations is higher in the wake region and behind the trailing edge where the vortices are shed and travel downstream. The addition of artificial viscosity, as shown in Figure 2a, efficiently dampens the vortices and consequently reduces the amplitude of acoustic waves far from the trailing edge.

B. Optimization

In this section, the noise at an observer located at a unit chord length above the trailing edge is reduced. A total of four design parameters are chosen. The maximum camber, c^a_{max}, the distance of maximum camber from the airfoil leading edge, $x_{c^a_{max}}$, maximum thickness of the airfoil t^a_{max}, and the angle of attack, α, are the four design parameters, i.e. $\boldsymbol{\mathcal{X}} = [c^a_{max}, x_{c^a_{max}}, t^a_{max}, \alpha]$, depicted in Figure 4. The simulation

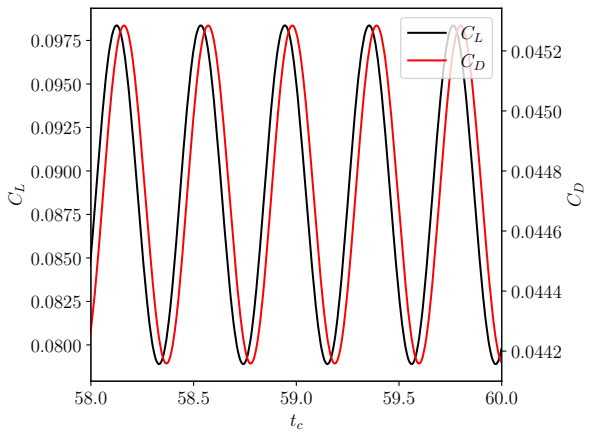

Figure. 3: Time-histories of lift and drag coefficients.

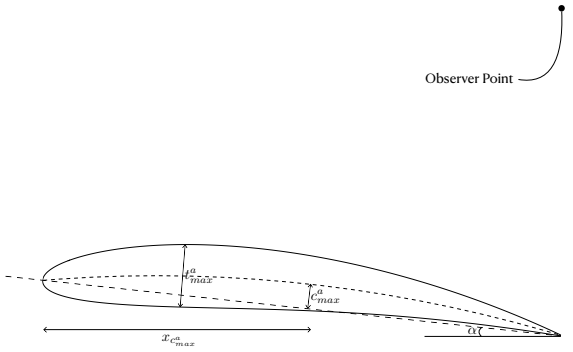

Figure. 4: The design variables and the observer point located at a unit chord length above the trailing edge for the two-dimensional NACA0012 airfoil.

is first run for 60 convective times for each objective function evaluation. Then the time-averaged pressure is computed from $20t_c$ to $40t_c$, $\overline{p}_{20-40}$, and then from $40t_c$ to $60t_c$, $\overline{p}_{40-60}$. If the difference between $\overline{p}_{20-40}$ and $\overline{p}_{40-60}$ is above one percent, the simulation is run for 20 more convective times. The simulation is run long enough so that the difference between two consecutive time-averaged pressure signal, over $20t_c$, is below one percent.

1) Results and Discussion: The optimization procedure is run using a maximum polynomial degree of $\mathcal{P}3$. The maximum camber range is set to $c^a_{max} \in [-10, 10]$ as a percentage of the chord, with the distance from the airfoil leading edge in the range of $x_{c^a_{max}} \in [2, 9]$ as a tenth of the chord. The maximum thickness of the airfoil is within the range of $t^a_{max} \in [8, 16]$ as a the percentage of the chord. Finally, the angle of attack varies from $-5°$ to $5°$. The objective function is defined as the sound pressure level at the observer with a constraint in the mean lift coefficient. A quadratic penalty term is added to the objective function when the lift coefficient is less than the baseline design, and a linear term is added when $\overline{C_L}$ is greater than the baseline design. The objective function is defined as

$$\mathcal{F} = \begin{cases} SPL + \epsilon_1 \left(\overline{C_L} - \overline{C_{L,baseline}}\right)^2 & \overline{C_L} < \overline{C_{L,baseline}} \\ SPL - \epsilon_2 \left(\overline{C_L} - \overline{C_{L,baseline}}\right) & \overline{C_L} \geq \overline{C_{L,baseline}} \end{cases}, \tag{10}$$

where the constants ϵ_1 and ϵ_2 are set to 40000 and 4, respectively, to compensate for the order of magnitude difference in SPL and $\overline{C_L}$.

This optimization procedure converges after 47 MADS iterations. The design space and the convergence of the objective function are shown in Figure 5. The optimal airfoil design has a maximum camber of $c^a_{max} = -0.209$ percent of the chord, at a 5.246 tenth of the chord distance from the leading edge, with a thickness of $t^a_{max} = 8.028$ percent of the chord, at an angle of attack of $\alpha = 2.786$ degrees. The optimized airfoil is silent with $SPL = 0$ dB, and $\overline{C_L} = 0.1647$, an increase of 88%. And, finally, the pressure perturbation and z-component

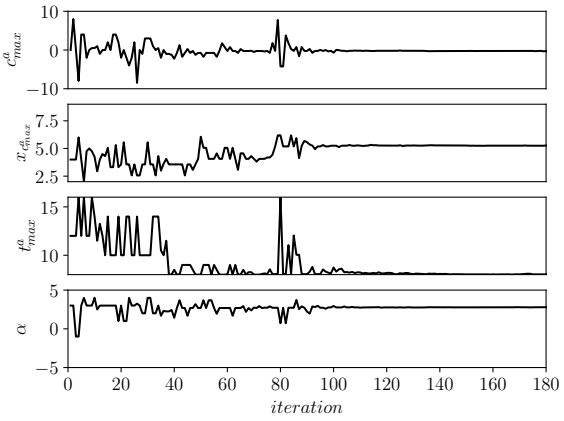

(a) The design space.

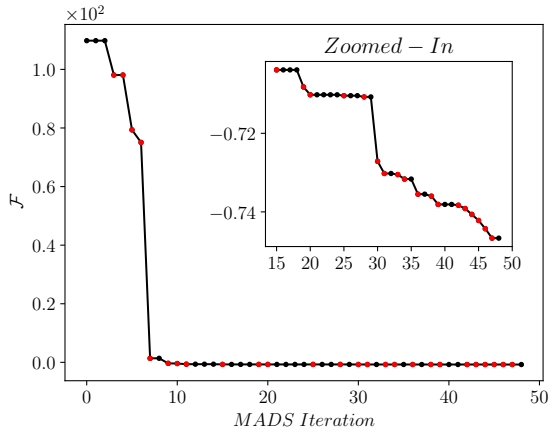

(b) The objective function convergence with the new incumbent design highlighted in red.

Figure. 5: The design space and objective function convergence for $\mathcal{P}3$ optimization of the NACA 4-digit airfoil.

of vorticity are shown in Figure 6 for the baseline and optimum designs. In the baseline design, the flow is attached to the airfoil on the pressure side, and flow instability occurs on the suction side. A periodic vortex shedding takes place as the flow passes over the trailing edge, resulting in acoustic wave generation. However, in the optimum design, the flow instability is eliminated resulting in a quiet airfoil.

IV. Conclusions

This paper demonstrates the efficacy of using the high-order flux reconstruction method, direct acoustic computation, and mesh adaptive direct search optimization technique for aero-acoustic shape optimization. The results showed that the approach could eliminate noise while increasing the lift coefficient by 88% for NACA 4-digit airfoil. These findings have practical applications in various industries, including aerospace, automotive, and wind turbine design, where noise reduction is crucial. In conclusion, this paper illustrates that MADS is an effective and robust gradient-free method for

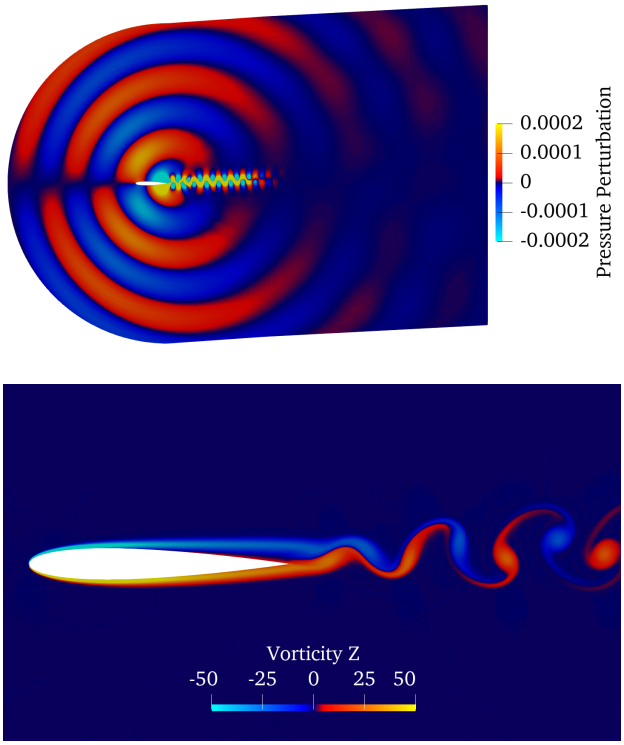

(a) The baseline design.

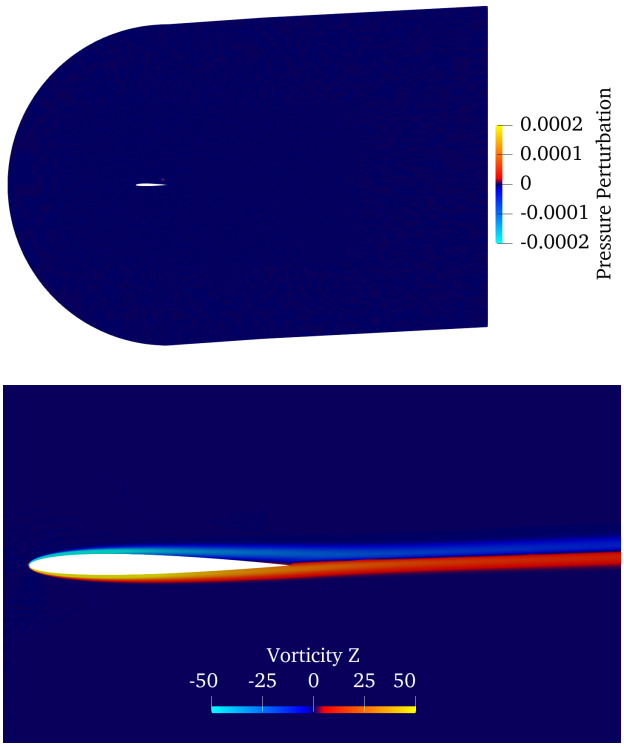

(b) The optimum design.

Figure. 6: The pressure perturbation and vorticity in the z-direction for the baseline and $\mathcal{P}3$ optimization designs of NACA0012 airfoil at $t_c = 60$.

solving complex aero-acoustic problems with high-order accuracy. Future work could extend this approach to more complex geometries, higher dimensions, and higher Reynolds numbers to explore the optimization technique's potential limits and expand its applications.

References

[1] World Health Organization et al. *Burden of disease from environmental noise: Quantification of healthy life years lost in Europe*. World Health Organization. Regional Office for Europe, 2011.

[2] Mathias Basner, Charlotte Clark, Anna Hansell, James I Hileman, Sabine Janssen, Kevin Shepherd, and Victor Sparrow. Aviation noise impacts: state of the science. *Noise & health*, 19(87):41, 2017.

[3] Christopher B Pepper, Marc A Nascarella, and Ronald J Kendall. A review of the effects of aircraft noise on wildlife and humans, current control mechanisms, and the need for further study. *Environmental Management*, 32:418–432, 2003.

[4] Global outlook for air transport. Technical report, International Air Transport Association (IATA), June 2022.

[5] PL Roe. Technical prospects for computational aeroacoustics. *DGLR BERICHT*, pages 206–206, 1992.

[6] Christopher KW Tam. Computational aeroacoustics-issues and methods. *AIAA journal*, 33(10):1788–1796, 1995.

[7] Tim Colonius and Sanjiva K Lele. Computational aeroacoustics: progress on nonlinear problems of sound generation. *Progress in Aerospace sciences*, 40(6):345–416, 2004.

[8] Sanjiva K Lele and Joseph W Nichols. A second golden age of aeroacoustics? *Philosophical Transactions of the Royal Society A: Mathematical, Physical and Engineering Sciences*, 372(2022):20130321, 2014.

[9] Stéphane Moreau. The third golden age of aeroacoustics. *Physics of Fluids*, 34(3):031301, 2022.

[10] David A Kopriva and John H Kolias. A conservative staggered-grid chebyshev multidomain method for compressible flows. *Journal of computational physics*, 125(1):244–261, 1996.

[11] Zhi Jian Wang. Spectral (finite) volume method for conservation laws on unstructured grids. basic formulation: Basic formulation. *Journal of Computational Physics*, 178(1):210–251, 2002.

[12] Hung T Huynh. A flux reconstruction approach to high-order schemes including discontinuous Galerkin methods. In *18th AIAA Computational Fluid Dynamics Conference*, page 4079, 2007.

[13] BC Vermeire and PE Vincent. On the behaviour of fully-discrete flux reconstruction schemes. *Computer Methods in Applied Mechanics and Engineering*, 315:1053–1079, 2017.

[14] Peter Vincent, Freddie Witherden, Brian Vermeire, Jin Seok Park, and Arvind Iyer. Towards green aviation with python at petascale. In *SC'16: Proceedings of the International Conference for High Performance Computing, Networking, Storage and Analysis*, pages 1–11. IEEE, 2016.

[15] Zhi Jian Wang and Haiyang Gao. A unifying lifting collocation penalty formulation including the discontinuous Galerkin, spectral volume/difference methods for conservation laws on mixed grids. *Journal of Computational Physics*, 228(21):8161–8186, 2009.

[16] Robert W Paterson, Paul G Vogt, Martin R Fink, and C Lee Munch. Vortex noise of isolated airfoils. *Journal of Aircraft*, 10(5):296–302, 1973.

[17] Henri Arbey and J Bataille. Noise generated by airfoil profiles placed in a uniform laminar flow. *Journal of Fluid Mechanics*, 134:33–47, 1983.

[18] Takashi Atobe and Tomoaki Ikeda. Flow instability around a 2D airfoil induced by acoustic disturbances at low Reynolds numbers. In *Proc. 27th Congress of Int. Council of Aeronautical Sciences, Ëession*, volume 3, pages 1–13.

[19] Tomoaki Ikeda, Takashi Atobe, and Shohei Takagi. Direct simulations of trailing-edge noise generation from two-dimensional airfoils at low Reynolds numbers. *Journal of Sound and Vibration*, 331(3):556–574, 2012.

[20] Larry Trumbull Clark. The radiation of sound from an airfoil immersed in a laminar flow. 1971.

[21] Alan S Hersh and Richard E Hayden. Aerodynamic sound radiation from lifting surfaces with and without leading-edge serrations. Technical report, 1971.

[22] Christopher KW Tam. Discrete tones of isolated airfoils. *The Journal of the Acoustical Society of America*, 55(6):1173–1177, 1974.

[23] Alison L Marsden, Meng Wang, Bijan Mohammadi, and P Moin. Shape optimization for aerodynamic noise control. *Center for Turbulence Research Annual Brief*, pages 241–47, 2001.

[24] Alison L Marsden, Meng Wang, John E Dennis, and Parviz Moin. Optimal aeroacoustic shape design using the surrogate management framework. *Optimization and Engineering*, 5(2):235–262, 2004.

[25] J-C Jouhaud, Pierre Sagaut, Marc Montagnac, and Julien Laurenceau. A surrogate-model based multidisciplinary shape optimization method with application to a 2D subsonic airfoil. *Computers & Fluids*, 36(3):520–529, 2007.

[26] Tomoaki Ikeda and Takashi Atobe. Numerical studies of acoustic effects on 2D airfoil aerodynamics at a low Reynolds number. In *50th AIAA Aerospace Sciences Meeting including the New Horizons Forum and Aerospace Exposition*, page 700, 2012.

[27] Brian C Vermeire. Paired explicit runge-kutta schemes for stiff systems of equations. *Journal of Computational Physics*, 393:465–483, 2019.